

CrossMark
click for updatesCite this: *J. Mater. Chem. A*, 2015, 3, 19148

A facile route to the synthesis of reduced graphene oxide-wrapped octahedral Cu₂O with enhanced photocatalytic and photovoltaic performance†

Xueqin Liu,^{ab} Zhen Li,^{*a} Wen Zhao,^a Caixin Zhao,^a Yang Wang^a and Zhiqun Lin^{*b}

Reduced graphene oxide (rGO)-wrapped octahedral Cu₂O composites (GCCs) were successfully produced by an ultrasonication-assisted reduction of graphene oxide (GO) in the Cu₂O precursor solution. During the ultrasound reaction, the reduction of GO and the growth of octahedral Cu₂O crystals occurred simultaneously in conjunction with the deposition of Cu₂O crystals on graphene. As a result of the introduction of rGO, the light absorption of octahedral Cu₂O was markedly improved, the size of Cu₂O crystals was decreased, and the self-aggregation of Cu₂O crystals was effectively prevented. More importantly, the charge separation and transfer were effectively enhanced. Compared to the pure octahedral Cu₂O crystals and commercial TiO₂ (P25), the GCCs exhibited an increased degradation rate of methyl orange (MO) by 4.5 and 20.2 times, respectively. Meanwhile, upon the graphene loading, the photoelectric conversion efficiency of GCC electrodes was largely improved resulting in an efficiency of 0.151%, representing an 8 fold higher efficiency than that of pure Cu₂O crystals.

Received 19th July 2015
Accepted 12th August 2015

DOI: 10.1039/c5ta05508c

www.rsc.org/MaterialsA

1. Introduction

Recent research has witnessed rapid advances in syntheses of nanostructured semiconductors of different sizes, shapes and compositions for use in photocatalysis, light-emitting diodes, solar cells, lithium ion batteries, and chemical sensors.^{1–3} Among a large variety of metal oxide semiconductors, cuprous oxide (Cu₂O) as an intriguing p-type semiconductor with a band gap of 1.9–2.2 eV has garnered increased attention, due to its higher absorption coefficient and minority carrier diffusion length in the visible region, making Cu₂O an attractive candidate material for photocatalysis and photovoltaics. The theoretical photon-to-electron conversion efficiency of Cu₂O is 20%.⁴ Moreover, Cu₂O is abundant and nontoxic, and has low production cost.^{5–7} However, there are intrinsic drawbacks of Cu₂O, including the instability in wet air, photo-corrosion under light irradiation, particularly the fast recombination of the photo-generated electron-hole pairs, which lead to the deactivation of Cu₂O and thus limit its practical applications. Much work has been concentrated on the reduction of the recombination of electrons and holes by coupling Cu₂O nanoparticles with other materials, such as noble metals,⁸ semiconductor nanoparticles,^{9,10} carbon materials,^{11,12} etc.

In the latter context, carbon nanostructures such as carbon nanotubes and graphene offer new opportunities to develop nanocomposites with unusual electro-catalytic properties. Graphene has been widely recognized as a rising star in the carbon family, because of its unique properties and a diverse set of potential applications. Among its various exciting characteristics, the unique structural and electronic properties of graphene, including the giant 2D structure, high surface area, and high mobility of charge carriers, render it an excellent electron-transport material in the photocatalytic and photo-electrochemical processes.^{13,14} In addition, the surface properties of graphene can be modified through chemical methods, making its use in composites possible.² Thus, various forms of graphene-based nanocomposites have been investigated, most of which are proposed for catalytic and electronic applications.¹⁵

Recently, materials produced by combining rGO with metal oxide semiconductors have emerged as promising products for a wide range of potential applications in electronic devices, drug delivery, photocatalysis, energy conversion and storage.^{16–18} Notably, the attachment of metal oxide nanoparticles onto graphene may also prevent the restacking and agglomeration of graphene sheets due to van der Waals interactions between them during the reduction process. Some studies have been carried out in the synthesis of rGO/Cu₂O composites and their applications in electrocatalysts for oxygen reduction reactions, supercapacitors, and lithium ion batteries.^{19–21} In contrast, the work on the implementation of GCCs in photocatalysis is comparatively few,²² and surprisingly,

^aFaculty of Materials Science and Chemistry, China University of Geosciences Wuhan, Hubei 430074, China. E-mail: zhenli@cug.edu.cn

^bSchool of Materials Science and Engineering, Georgia Institute of Technology, Atlanta, GA 30332, USA. E-mail: zhiqun.lin@mse.gatech.edu

† Electronic supplementary information (ESI) available. See DOI: 10.1039/c5ta05508c

there is no report on the photovoltaic performance of rGO/Cu₂O composites.

Herein, we report on a viable strategy for crafting rGO-wrapped octahedral Cu₂O composites (GCCs) at low temperature by capitalizing on, for the first time, ultrasonication, without the need for the application of surfactants as in copious past work. The rGO sheets not only provide a large surface area that is accessible for target molecules, but also serve as anchoring spots for the deposition of octahedral Cu₂O. The photocatalytic and photovoltaic performances of GCCs were evaluated and compared with those of pure octahedral Cu₂O particles, signifying the importance of the anchoring of octahedral Cu₂O particles on GO sheets. It is noteworthy that such an ultrasonication-based strategy is simple yet effective, imparting the effective hybridization (*i.e.*, interfacial contact) of graphene with Cu₂O, and thus improving the charge transport characteristics. As such, it opens up a new avenue creating rGO-wrapped semiconductor composites for a variety of energy conversion and storage applications.

2. Experimental

2.1 Preparation of rGO/octahedral Cu₂O composites (GCCs)

The fabrication of GCCs is schematically shown in Fig. 1. The graphene oxide (GO) sheets were first synthesized by a modified Hummers' method.²³ In a typical synthesis of rGO-Cu₂O, 50 mg of GO sheets was dispersed in 100 mL 0.25 M CuSO₄ solution by ultrasonication for 30 min, resulting in a green mixture. 100 mL 1 M NaOH was then added into the above solution. The color of solution turned dark blue quickly. After ultrasonication for 15 min, 1.5 mL NH₂OH·HCl was added into the blue solution. The reaction mixture was then treated with high-intensity ultrasound (100 W, 40 kHz) at room temperature in air for a certain period of time. The reduction of GO was also confirmed from the color change of the solution before and after reduction (from brown to dark, as shown in the inset of Fig. 1). Subsequently, the resulting black solid was centrifuged, washed and dried in a vacuum at 60 °C for 3 h prior to characterization. Pure Cu₂O was also obtained by a similar process in the absence of GO.

2.2 Characterization

The phase and composition of products were determined by using a Dmax-3β diffractometer with nickel-filtered Cu Kα radiation ($\lambda = 1.54178 \text{ \AA}$). The size and morphology of samples

were investigated by field emission scanning electron microscopy (FESEM; JEOL-6300F) and energy dispersive spectroscopy (EDS). Transmission electron microscopy (TEM) was conducted on a Tecnai F20 microscope (FEI Corp.). Fourier transform infrared spectroscopy (FTIR) spectra were recorded on an Equinox 55 spectrophotometer. The measurements were performed in solid phase using KBr pellets. An ultraviolet-visible (UV-Vis) spectrophotometer Perkin-Elmer Lambda 35 was used to carry out the UV-Vis absorption measurement on the samples. Raman spectroscopy was performed by using a RFS 100/s Bruker NIR-FT spectrophotometer in the range from 500 to 2000 cm⁻¹.

2.3 Photocatalytic measurements

In a typical reaction, 40 mg of rGO/Cu₂O composites (GCCs) was added to 40 mL methyl orange (MO) solution (concentration, $c = 20 \text{ mg L}^{-1}$). The suspension was first magnetically stirred in the dark for 0.5 h to ensure the establishment of the adsorption/desorption equilibrium of MO onto the surface of GCC photocatalysts. Subsequently, the suspension was placed under visible-light. At various time intervals, a portion of the mixture was taken, separated magnetically and analyzed with a UV-Vis spectrophotometer to evaluate the catalytic degradation of MO with a UV-2401 spectrophotometer. For comparison, the photocatalytic activity of pure Cu₂O and P25 was also detected by the same approach.

2.4 Photoelectrochemical measurements

Briefly, the GCCs and pure Cu₂O particles were deposited as a thin film onto Fluorine-doped Tin Oxide (FTO) by spin coating a suspension of this powder in ethanol, respectively, which were used as photoanodes in solar cells. The solar cells were assembled in a typical sandwich type by placing a platinum-coated conducting glass on the dye-sensitized photoanode separated by using a *ca.* 50 mm polymer spacer. The active area of the cell was $5 \times 5 \text{ mm}^2$. An electrolyte was prepared with 1.0 M 1-butyl-3-methylimidazolium iodide (BMIMI), 50 mM LiI, 30 mM I₂ and 0.5 M *tert*-butylpyridine in a mixed solvent of acetonitrile and valeronitrile. The photocurrent tests and the photocurrent–voltage (I - V) characteristics of the obtained materials were measured using the electrochemical workstation (CHI660C, Chenhua, China). The light was produced by using a solar simulator (Newport, Oriel class A) at 100 mW cm^{-2} (1 sun) intensity. Electrochemical impedance spectroscopy (EIS) measurements were also performed on the same electrochemical workstation over a frequency range from 0.01 Hz to 100 kHz at the open-circuit voltage.

3. Results and discussion

The morphology, size and microstructure of pure Cu₂O particles and as-prepared GCCs (Fig. 1 in the Experimental section) were scrutinized by SEM and TEM. The FESEM images in Fig. 2a clearly show the octahedral morphology of pure Cu₂O particles with an average edge length of approximately 150 nm. After modifying the Cu₂O particle surface with rGO, the morphology

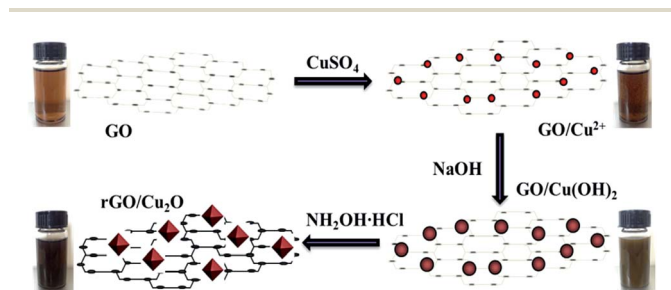


Fig. 1 Schematic illustration of synthesis of rGO-wrapped octahedral Cu₂O composites (*i.e.*, GCCs; that is rGO/Cu₂O composites).

of the final materials is shown in Fig. 2b–d. In contrast to the previous study where small Cu_2O nanoparticles (<50 nm) were dispersed on rGO,²⁴ in this work rGO was loaded on large Cu_2O particles, yielding rGO-wrapped octahedral Cu_2O composites. Notably, the loading mechanism is governed by the relative size of materials,²⁵ where smaller rGO tends to be loaded on larger Cu_2O particles and smaller Cu_2O particles tend to be deposited on larger rGO. Moreover, Cu_2O particles were well separated from each other and dispersed by rGO. In contrast, pure Cu_2O octahedra were slightly aggregated, as shown in Fig. 2a. It is interesting to note the rGO served as an additional surfactant, the size of Cu_2O particles (approximately 100 nm) wrapped by graphene was smaller than that of pure Cu_2O particles.

Fig. 3a shows the XRD patterns of GO, Cu_2O particles and GCCs. For GO, the dominant diffraction peak at 10.4° corresponds to the (002) interlayer spacing of 0.83 nm, which can be ascribed to the fact that graphite was considerably oxidized. Notably, the GCCs displayed a similar crystalline structure to that of pure octahedral Cu_2O particles, which can be indexed to the standard Cu_2O nanocrystal with a cubic structure (JCPDS 05-0667). However, the peak intensity of the (111) plane for GCCs became weaker than that for pure octahedral Cu_2O particles, indicating that the growth of the (111) plane was inhibited due to the presence of rGO. Moreover, no peaks for graphite at $2\theta = 26.3^\circ$, corresponding to the (002) plane, can be observed, suggesting no further agglomeration of few-layer rGO sheets as they were hindered by the presence of Cu_2O particles. Furthermore, the diffraction peak of GO at $2\theta = 10.4^\circ$ cannot be observed, signifying the reduction of GO. To further confirm that it was octahedral Cu_2O loaded on the rGO sheets, the corresponding energy-dispersive X-ray (EDX) measurement on the composites was also performed (Fig. S1, ESI†). There were only Cu, O and C seen in the composites, verifying the existence of Cu_2O on the surface of rGO.

Fig. 3b compares the FTIR spectra of GO, Cu_2O and GCCs samples. In the case of GO, the peaks at 1625 and 1739 cm^{-1} are attributed to the O–H bending vibration and the C=O

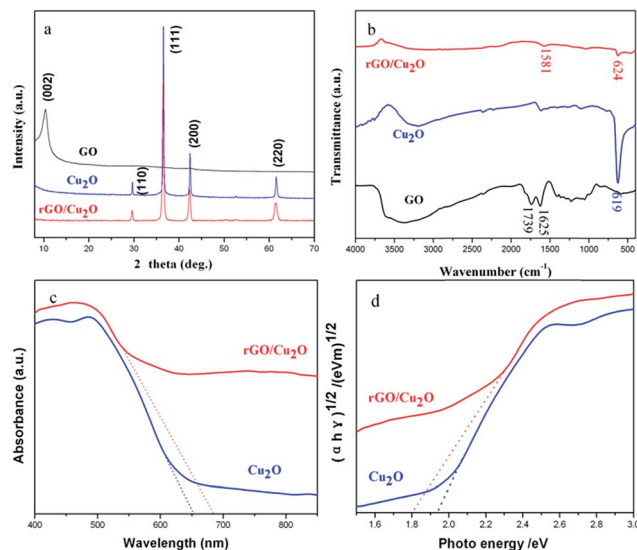


Fig. 3 (a) XRD patterns and (b) FTIR spectra of the as-prepared GO, Cu_2O particles and GCCs, respectively. (c) UV-Vis spectra and (d) $(\alpha h\nu)^{1/2}$ as a function of photon energy of the Cu_2O particles and GCCs, respectively.

stretching of the COOH group, respectively. As for GCCs, the GO peaks were not observed, suggesting that the reduction of GO to rGO was completed by $\text{NH}_2\text{OH}\cdot\text{HCl}$ in an alkaline environment. The intense absorption bands at 624 and 1581 cm^{-1} can be assigned to the Cu–O stretching vibration in the Cu_2O phase and the C=C skeletal vibration of rGO, respectively.

The UV-Vis absorption spectra of pure Cu_2O particles and GCCs are shown in Fig. 3c. Obviously, the pure Cu_2O exhibited an absorbance in the visible region with a broad absorbance peak at approximately 550 nm . Compared to pure Cu_2O particles, the GCCs displayed an enhanced absorbance in the entire visible region, with a 30 nm red shift in the absorption edge, which can be attributed to the presence of rGO in GCCs, similar to the study on carbon-doped TiO_2 composites.²⁶ Thus, the photocatalytic activity is expected to be enhanced, and the solar energy may be utilized more efficiently. Moreover, the plot of $(\alpha h\nu)^{1/2} \sim h\nu$ was constructed to estimate the band gap of the as-prepared materials, where $\alpha = (1 - R)^2/2R$, where $R = 10^{-4}$ and A is an optical absorption.²⁷ The band gap of photocatalysts can be calculated by extrapolating the linear section. The band gap of pure octahedral Cu_2O particles was estimated to be 1.94 eV , whereas the band gap of GCCs was slightly reduced to 1.77 eV , as shown in Fig. 3d. The formation of Cu–O–C may result in the up-shift of the valence band edge, thereby reducing the band gap.

Raman spectroscopy is widely recognized as a versatile tool for the characterization of rGO as it can identify the number of layers, the electronic structure, the type of doping, and any defects in rGO.²⁸ Raman spectroscopy measurements were conducted to confirm the formation of GCCs, and to further analyze the reduction of GO. The characteristic Raman peaks of graphite, GO and GCCs are shown in Fig. 4. The Raman spectrum of rGO was characterized by two main features: the G band is usually assigned to the E_{2g} phonon of C sp^2 atoms, while the D band is a breathing mode of κ -point photons of A_{1g} symmetry,

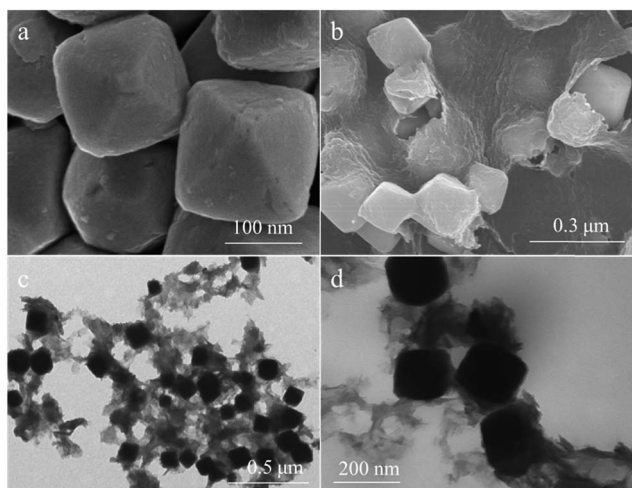


Fig. 2 (a and b) FESEM and (c and d) TEM images of pure Cu_2O and GCCs.

which is a common feature of sp^3 defects in carbon.²⁹ Therefore, the amount of defects could be conveniently compared by the relative peak intensity ratios of D to G bands (I_D/I_G). As shown in Fig. 4a, the Raman spectrum of the pristine graphite displayed a strong G band at 1572 cm^{-1} and a weak D band at 1340 cm^{-1} . In the Raman spectrum of GO (Fig. 4b), the G band was broadened and blue-shifted to 1594 cm^{-1} due to the presence of isolated double bonds that resonate at higher frequencies than the G band of pristine graphite.³⁰ Additionally, the intensity ratio (I_D/I_G) for GO (0.995) was much higher than that for graphite (0.217), indicating the presence of carbonaceous defects or edge areas in the GO sheets due to the oxidation of graphite. For the GCC composite (Fig. 4c), the I_D/I_G ratio was further increased to 1.054, suggesting the formation of more sp^3 defects in carbon. The increased ratio of D/G intensity was indicative of the successful reduction of GO to rGO. The possible reason for the increased sp^3 defects can be attributed to the strong interaction (e.g., the Cu–O–C bond) between the interface of Cu_2O octahedra and rGO nanosheets.

To investigate the effect of rGO loading on photocatalytic performance, photocatalysis experiments of GCCs, pure octahedral Cu_2O particles and P25 (commercially available TiO_2 nanoparticles) were carried out by the degradation of MO dye under visible light. Fig. 5a shows the changes in the optical spectra of the MO solution at different intervals when the GCCs were added. The intensity of the absorption peak at 464 nm of MO decreased sharply as the time progressed, indicating that the GCCs possessed a significant photocatalytic ability for organic dye (i.e., MO molecules). Fig. 5b compares the relative concentration variations of the MO solution over 50 min using GCCs, pure octahedral Cu_2O particles and P25, respectively. The pure octahedral Cu_2O particles outperformed P25 in the photodegradation of MO, and the GCCs further improved the photocatalytic performance over that of the Cu_2O particles. A simple calculation of the first-order degradation rate constant (κ) for these materials was quantitatively evaluated according to $\kappa = -\ln(C/C_0)/t$, as shown in Fig. 5c. The degradation rate of GCCs was much improved as compared to that of the un-modified octahedral Cu_2O particles (by a factor of 4.5) and P25 (by a factor of 20.2). Clearly, a markedly enhanced degradation rate was found upon the surface modification of Cu_2O particles with rGO nanosheets. Such largely improved photocatalytic activity of GCCs can probably be attributed to the enhanced light absorbance and the extended light absorption range (Fig. 3c). Additionally, in comparison with pure Cu_2O particles, the larger surface of GCCs can offer more active adsorption sites, resulting in enhanced adsorptivity of contaminant molecules (Fig. S2, ESI†). It is not surprising that when Cu_2O particles are coupled with rGO, the photo-generated electrons can easily transfer to rGO, leading to the enhanced charge separation, which is crucial in enhancing the photocatalytic reactivity.

Due to the importance of stability of a photocatalyst for its practical application,³¹ the photocatalytic stability of GCCs was further investigated by the cycling experiment. As shown in Fig. 5d, the photocatalytic efficiency of GCCs exhibited no visible change after five recycles, reflecting that the GCC

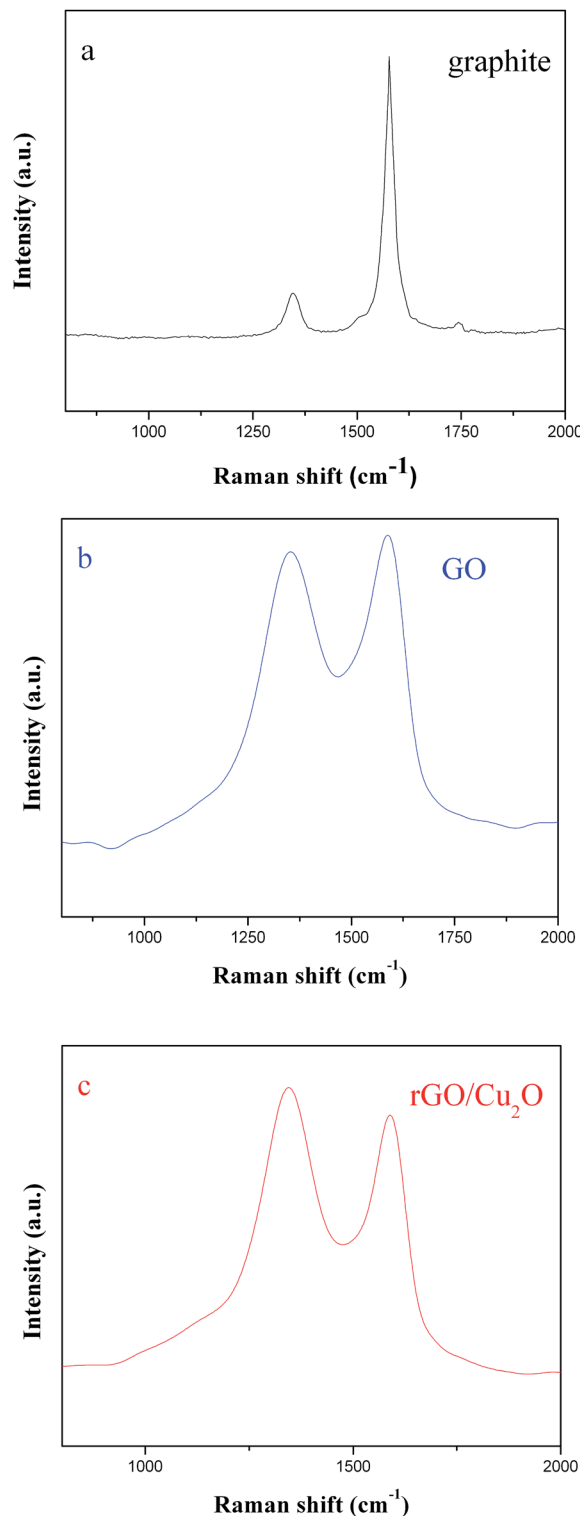


Fig. 4 Raman spectra of (a) graphite, (b) GO, and (c) GCCs.

photocatalyst possessed a good reusability. In addition, due to the incorporation of rGO, the GCC particles may easily and quickly settle down from the dye solution, which is beneficial for the collection of photocatalysts.

To evaluate the photoelectrochemical properties of GCCs, a series of photoelectrochemical experiments were performed.

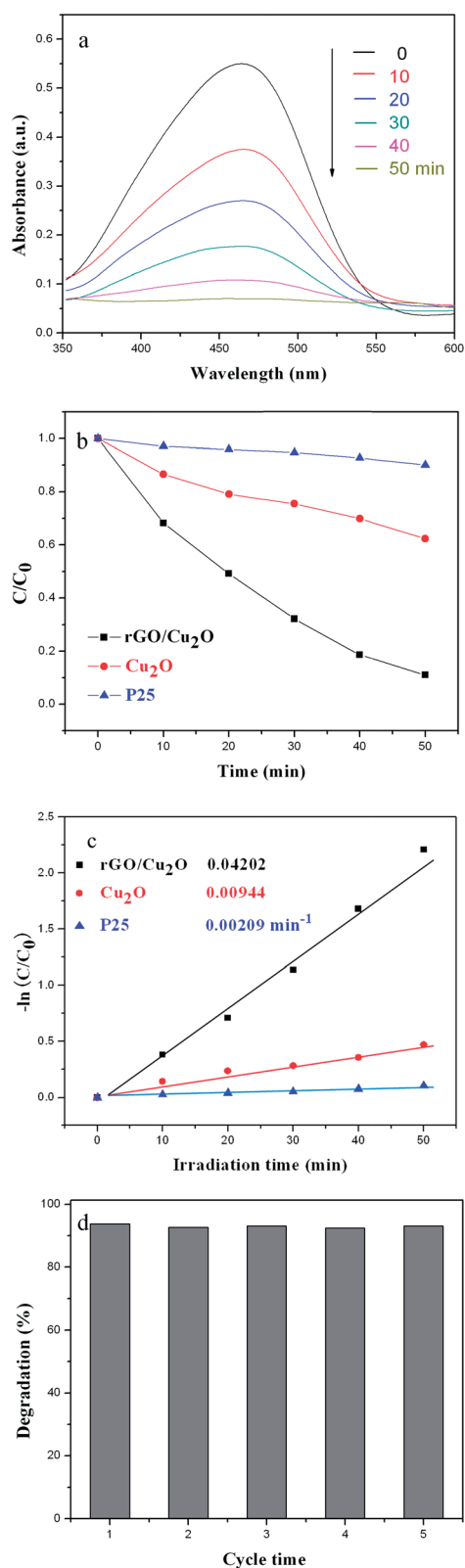


Fig. 5 (a) UV-visible absorption spectra of degradation of MO by GCCs. (b) Comparison of photocatalytic degradation of MO by different photocatalysts. (c) The degradation rate constants from different photocatalysts. (d) The stability test of GCCs.

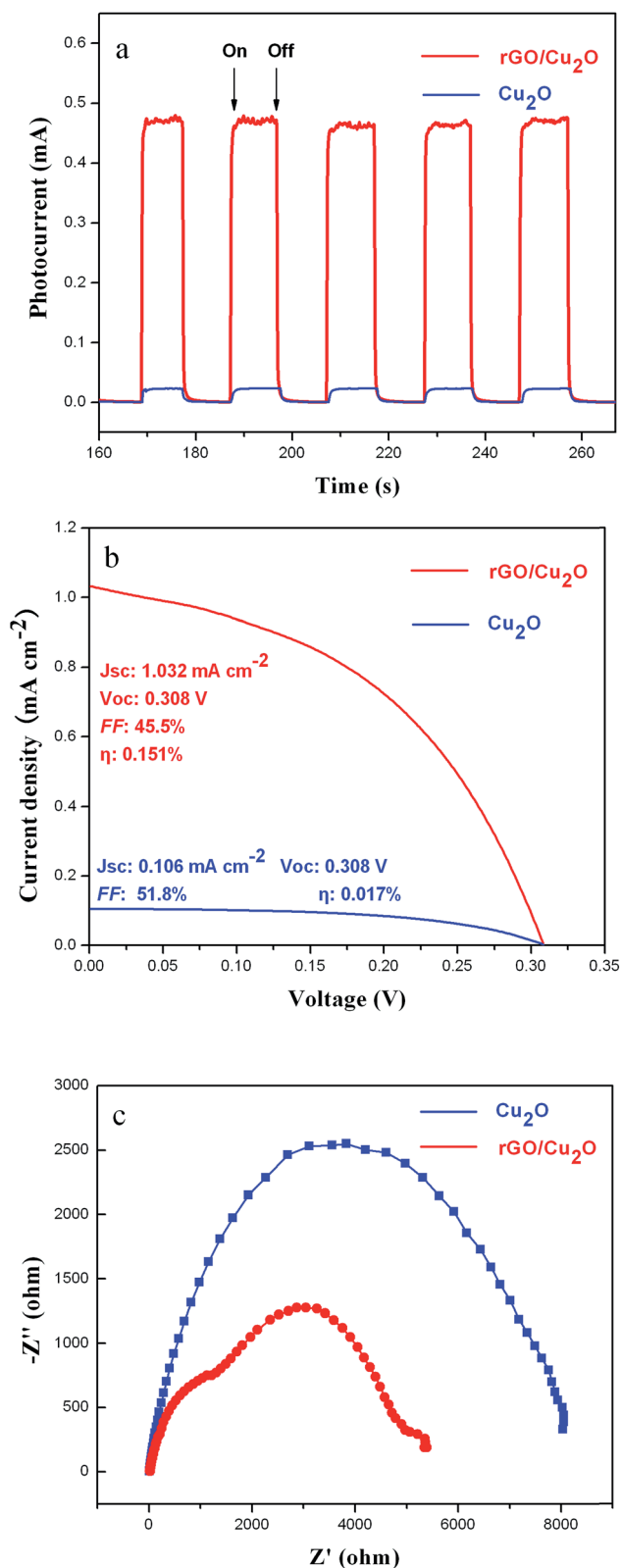


Fig. 6 (a) The current as a function of time; (b) the current density–voltage characteristics; (c) electrochemical impedance spectra of Cu₂O and rGO/Cu₂O, respectively.

Fig. 6a presents the photocurrent density–time characteristics for pure Cu₂O and GCC electrodes. Remarkably, as expected, the GCCs were indeed able to generate a significant photocurrent. Specifically, the photocurrent density of GCC electrodes was about 0.46 mA cm⁻², which is nearly 23 times higher than that achieved by the pure Cu₂O electrode (0.02 mA cm⁻²). The higher photocurrent density of GCC photoelectrodes was indicative of an improved optical absorption capability and an enhanced separation of photogenerated electrons and holes as compared to pure Cu₂O. The typical current density–voltage (*J*–*V*) curves of Cu₂O and GCC electrodes during illumination are shown in Fig. 6b. It should be noted that the open-circuit voltage (*V*_{OC}) was maintained at 0.308 V. As graphene is a zero band gap material, the incorporation of rGO does not show much effect on the apparent Fermi level of Cu₂O.^{32,33} As a result, the value of *V*_{OC} remained the same. Interestingly, the short circuit current density (*J*_{SC}) and conversion efficiency (*η*) of pure Cu₂O were very low, which are 0.106 mA cm⁻² and 0.017%, respectively. In sharp contrast, the *η* of GCC was 0.151% with a *J*_{SC} of 1.032 mA cm⁻². Compared to the octahedral Cu₂O, it is remarkable that an 800% increase in *η* was obtained. This was consistent with the results of the photocurrent response, suggesting that rGO can act as an electron acceptor to effectively improve the photovoltaic performance of the Cu₂O photocathode. In order to gain insight into the enhanced photovoltaic performance by implementing the GCCs, the electrochemical impedance spectroscopy (EIS) measurements on GCCs and pure Cu₂O were performed at a potential of –3.0 mV over the frequency range from 100 kHz to 0.01 Hz (Fig. 6c). Both impedance curves showed a semicircle in the intermediate frequency region. The diameter of this semicircle can be attributed to the charge transfer resistance (*R*_{ct}). Clearly, the semicircle diameter of GCCs is much smaller than that of pure Cu₂O, suggesting that the GCCs possessed a lower charge transfer resistance, thereby leading to the increased photo-current conversion efficiency.

4. Conclusions

In summary, we developed a facile strategy for synthesizing rGO-wrapped octahedral Cu₂O composites (GCCs) *via* an ultrasonication-assisted reduction of graphene oxide (GO) in the Cu₂O precursor solution at low temperature. Compared to pure octahedral Cu₂O, the resulting GCCs comprised smaller sized Cu₂O particles, and exhibited a good dispersion of Cu₂O particles and a largely improved light absorption. More importantly, in comparison with pure octahedral Cu₂O and P25, the presence of rGO effectively facilitated the charge separation and transfer in GCCs, thereby leading to a much increased degradation rate of methyl orange by 4.5 and 20.2 times, respectively. Quite intriguingly, it was demonstrated for the first time that the introduction of rGO into Cu₂O can markedly improve the photovoltaic performance of Cu₂O. The GCC electrodes showed a photoelectric conversion efficiency of 0.151%, which was 800% higher than that of pure Cu₂O particles (0.017%). Clearly, such an ultrasonication-based strategy is simple and easy to implement. Thus, it offers a particularly versatile way of creating

rGO-wrapped semiconductor composites for a diversity of energy conversion and storage applications.

Acknowledgements

X. Q. Liu acknowledges the financial support from the China Scholarship Council.

References

- 1 I. Concina and A. Vomiero, *Small*, 2015, **11**, 1744–1774.
- 2 L. Ding, Y. E., L. Fan and S. Yang, *Chem. Commun.*, 2013, **49**, 6286–6288.
- 3 H. Zhang, X. Lv, Y. Li, Y. Wang and J. Li, *ACS Nano*, 2009, **4**, 380–386.
- 4 L. Olsen, F. Addis and W. Miller, *Sol. Cells*, 1982, **7**, 247–279.
- 5 J. Cui and U. J. Gibson, *J. Phys. Chem. C*, 2010, **114**, 6408–6412.
- 6 F. Shao, J. Sun, L. Gao, J. Luo, Y. Liu and S. Yang, *Adv. Funct. Mater.*, 2012, **22**, 3907–3913.
- 7 D. Snoko, *Science*, 2002, **298**, 1368–1372.
- 8 L. Zhang, D. A. Blom and H. Wang, *Chem. Mater.*, 2011, **23**, 4587–4598.
- 9 T. Jiang, T. Xie, L. Chen, Z. Fu and D. Wang, *Nanoscale*, 2013, **5**, 2938–2944.
- 10 M. Wang, L. Sun, Z. Lin, J. Cai, K. Xie and C. Lin, *Energy Environ. Sci.*, 2013, **6**, 1211.
- 11 H. Wang, H. Feng and J. Li, *Small*, 2014, **10**, 2165–2181.
- 12 K. Woan, G. Pyrgiotakis and W. Sigmund, *Adv. Mater.*, 2009, **21**, 2233–2239.
- 13 J. Y. Lin, C. Y. Chan and S. W. Chou, *Chem. Commun.*, 2013, **49**, 1440–1442.
- 14 J. Zhang, Z. Xiong and X. S. Zhao, *J. Mater. Chem.*, 2011, **21**, 3634.
- 15 T. Sreeprasad, S. M. Maliyekkal, K. Lisha and T. Pradeep, *J. Hazard. Mater.*, 2011, **186**, 921–931.
- 16 S. Chen, J. Zhu, X. Wu, Q. Han and X. Wang, *ACS Nano*, 2010, **4**, 2822–2830.
- 17 M. Dutta, S. Sarkar, T. Ghosh and D. Basak, *J. Phys. Chem. C*, 2012, **116**, 20127–20131.
- 18 N. Li, G. Zhou, R. Fang, F. Li and H. M. Cheng, *Nanoscale*, 2013, **5**, 7780–7784.
- 19 B. Li, H. Cao, G. Yin, Y. Lu and J. Yin, *J. Mater. Chem.*, 2011, **21**, 10645.
- 20 C. Xu, X. Wang, L. Yang and Y. Wu, *J. Solid State Chem.*, 2009, **182**, 2486–2490.
- 21 X. Y. Yan, X. L. Tong, Y. F. Zhang, X. D. Han, Y. Y. Wang, G. Q. Jin, Y. Qin and X. Y. Guo, *Chem. Commun.*, 2012, **48**, 1892–1894.
- 22 P. D. Tran, S. K. Batabyal, S. S. Pramana, J. Barber, L. H. Wong and S. C. Loo, *Nanoscale*, 2012, **4**, 3875–3878.
- 23 W. S. Hummers Jr and R. E. Offeman, *J. Am. Chem. Soc.*, 1958, **80**, 1339.
- 24 L. Zhou, F. Shen, X. Tian, D. Wang, T. Zhang and W. Chen, *Nanoscale*, 2013, **5**, 1564–1569.
- 25 G. Lui, J.-Y. Liao, A. Duan, Z. Zhang, M. Fowler and A. Yu, *J. Mater. Chem. A*, 2013, **1**, 12255.

- 26 W. Ren, Z. Ai, F. Jia, L. Zhang, X. Fan and Z. Zou, *Appl. Catal., B*, 2007, **69**, 138–144.
- 27 H. Lin, C. Huang, W. Li, C. Ni, S. Shah and Y. Tseng, *Appl. Catal., B*, 2006, **68**, 1–11.
- 28 X. Liu, R. Cong, L. Cao, S. Liu and H. Cui, *New J. Chem.*, 2014, **38**, 2362.
- 29 P. Wang, J. Wang, X. Wang, H. Yu, J. Yu, M. Lei and Y. Wang, *Appl. Catal., B*, 2013, **132–133**, 452–459.
- 30 Z. Zhang, W. Yang, X. Zou, F. Xu, X. Wang, B. Zhang and J. Tang, *J. Colloid Interface Sci.*, 2012, **386**, 198–204.
- 31 M. Liu, R. Liu and W. Chen, *Biosens. Bioelectron.*, 2013, **45**, 206–212.
- 32 M. Freitag, *Nat. Nanotechnol.*, 2008, **3**, 455–457.
- 33 Z. Peining, A. S. Nair, P. Shengjie, Y. Shengyuan and S. Ramakrishna, *ACS Appl. Mater. Interfaces*, 2012, **4**, 581–585.